Electronic Supplementary Information (ESI)

Synthesis of new M-layer solid-solution 312 MAX phases $(Ta_{1-x}Ti_x)_3AlC_2$ (x = 0.4, 0.62, 0.75, 0.91 or 0.95), and their corresponding MXenes

Maxwell T. P. Rigby-Bell,[a] Varun Natu,[b] Maxim Sokol,[b,c] Daniel J. Kelly,[a] David G. Hopkinson,[a] Yichao Zou,[a] James R. T. Bird,[a] Lee J. Evitts,[d] Matt Smith,[a] Christopher P. Race,[a] Philipp Frankel,[a] Sarah J. Haigh*[,a] and Michel W. Barsoum*[,b]

[a.] ***Department of Materials, University of Manchester, Manchester, M13 9PL, UK***

[b.] ***Department of Materials Science & Engineering, Drexel University, Philadelphia, PA 19104, USA Email:***

[c.] ***Department of Materials Science and Engineering, Tel Aviv University, Ramat Aviv 6997801, Israel***

[d.] ***Nuclear Futures Institute, Bangor University, Gwynedd, LL57 2DG, UK***

* ***Corresponding author email:*** ***sarah.haigh@manchester.ac.uk***

* ***Co-corresponding author email:*** ***barsoumw@drexel.edu***

1 Density functional theory

To guide synthesis investigations, the enthalpy of formation, i.e. the thermodynamic stability relative to atomic constituents, of $TaTi_2AlC_2$, for two M-layer ordering and two A-layer stacking configurations (four different unit cells, as shown in Fig. S1) was calculated using first principles methods. To achieve this, the total ground state energy at zero Kelvin and zero pressure, E_{MAX}, was calculated along with those for individual elemental constituents, $E_{element}$, in equilibrium phase under similar conditions. The formation enthalpy of the phase, $\Delta H_{f,MAX}$ was then obtained using Hess' law:

$$\Delta H_{(f,MAX)} = E_{MAX} - \sum E_{element} \quad (1)$$

Total energy calculations were performed for supercells of 2×2×1 unit cells using density functional theory (DFT) as implemented in the Vienna ab initio simulation package (VASP).[1,2] A plane-wave basis set cut-off energy of 500 eV was used for all calculations, with electron-ion interactions represented using the projector augmented-wave (PAW) method.[3] The generalized gradient approximation (GGA)[4] was used in the form of the parameterisation proposed by Perdew, Burke, and Ernzerhof (PBE)[5,6] to represent the electronic exchange-correlation energy. Brillouin zone k-point sampling integrations were applied using a 3×3×1 Monkhorst-Pack grid,[7] resulting in a k-point spacing of at most 0.5 A^{-1}. Unit cells were relaxed until the forces on ions converged to < 0.1 meV/Å.

The $TaTi_2AlC_2$ configurations considered are shown in Fig. S1. The respective enthalpies of formation, ΔH_f, are shown in Fig. S2. A negative ΔH_f value in this context indicates thermodynamic stability relative to elemental

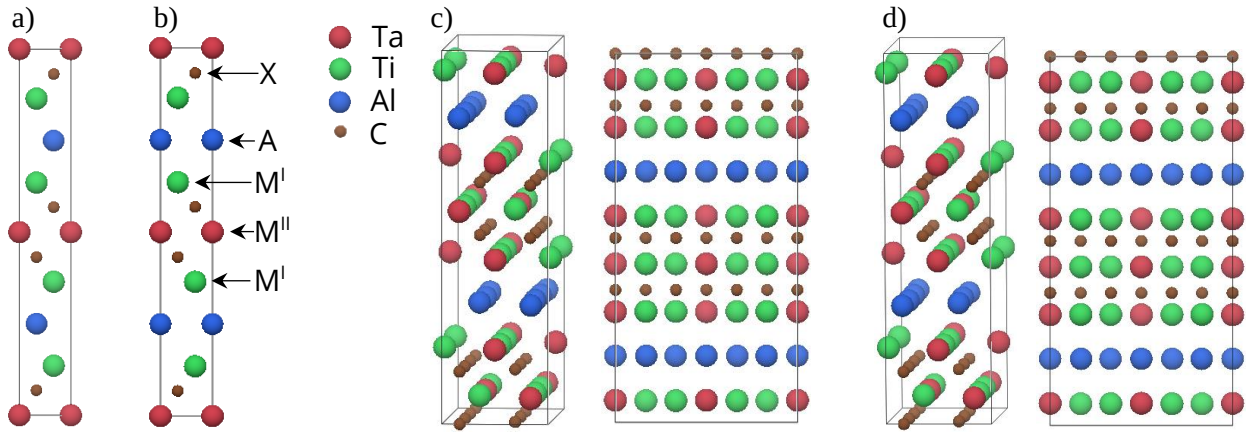

Fig. S1 Structural variations of $TaTi_2AlC_2$ for which total energy calculations were performed: a) α-$TaTi_2AlC_2$ (o-MAX), (b) β-$TaTi_2AlC_2$ (o-MAX), (c) α-$TaTi_2AlC_2$ (i-MAX-like), and (d) β-$TaTi_2AlC_2$ (i-MAX-like).

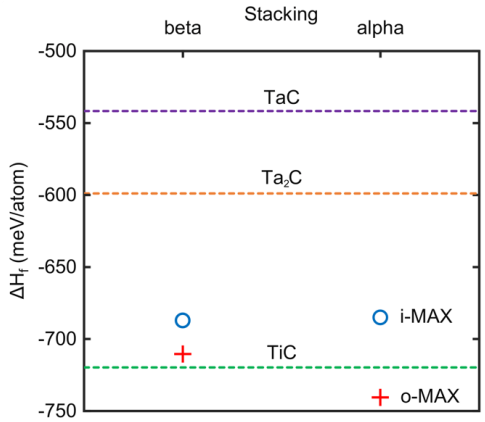

Fig. S2 The formation enthalpies (points), ΔH_f in meV/atom of the four $TaTi_2AlC_2$ unit cells in Fig. S1, with those of common binary carbide impurities (dashed lines) included for reference.

constituents at 0 K and is thus a step towards predicting actual stability. It is important to stress at this point that the aim of these calculations was to provide guidance in the search for new MAX phases, rather than to predict the existence of new stable phases with rigour. As such, the thermodynamic stability at expected synthesis temperatures (~1600 °C) and in relation to the set of 'most-competing phases' has not been considered as in recent calculations by Dahlqvist and Rosen.[8] For reference, ΔH_f values of common binary carbide impurities TaC, Ta_2C and TiC have been included in Fig. S2, as indicated by dashed horizontal lines. If a particular $TaTi_2AlC_2$ configuration falls below all of these lines, the phase is expected to be more thermodynamically stable and thus will have a higher propensity to form. All four MAX phase unit cells fall within 8% of the ΔH_f threshold of TiC at -719.74 meV/atom.

2 Synthesis

Powders of TaC, TiC, Ti and Al of mesh size at least –250 (maximum particle size 63 μm – see Table S1 for further information), were purchased from Alpha Aesar (Ward Hill, MA, USA). Powder mixtures in the molar ratios in Table S2 were zirconia ball milled in plastic jars for 12 h to provide a homogenous mixture. The latter was then uniaxially cold pressed at 250 MPa into compact 1.27 cm diameter pellets of mass ~10 g. The pellets were loaded into a 82 x 31 x 18 mm Al_2O_3 boat, covered with an Al_2O_3 plate, and placed inside an Al_2O_3 tube furnace with an inert flowing Ar atmosphere. Additionally, pure Ti powder was placed in an adjacent crucible upstream to the pellet as a residual oxygen getter. The furnace was then heated to 1600 °C at a rate of 5 °C/min and held for 8 h, before cooling to room temperature at a similar rate to the heating.

For MXene synthesis, a small region of the solid sintered $(Ta_{0.38}Ti_{0.62})_3Al_{0.81}C_2$ MAX phase pellet was milled using a TiN-coated bit. The milled powder was then passed through a 400 mesh (particle size < 38 μm) sieve. One gram of as-sieved MAX phase powder was then slowly added to a solution of 10 mL HCl (12M, Alfa Aesar, USA) and 1 g LiF (99.5%, 325 mesh, Alfa Aesar) at 20 °C and stirred for 12 h at 500 rpm. The resultant slurry was then transferred to a 50 mL centrifuge tube and deionised water was added to fill the remaining volume. It was then centrifuged at 3500 rpm for 60 s, with the resulting clear supernatant discarded. This washing procedure was repeated several times until the pH of the solution was ~7, at which point deionised water was added to the left-over sediment and the mixture sonicated under bubbling Ar flow for 1 h. Ice was added to the sonication bath to avoid oxidation. The solution was then centrifuged for 0.5 h at 3500 rpm and the supernatant was collected for further use. The sediments that are recovered after washing to pH 7 before sonication are referred to as multilayer, ML, powders. The MXene films obtained after vacuum filtering of the supernatant are referred to as delaminated MXene.

Table S1 Details of source material used for synthesis. *As quoted by the manufacturer.

Material	Purity (wt.%)*	Average particle size* (μm)
TaC	99.5	44
TiC	99.5	2
Ti	99.5	15
Al	99.5	15

Table S2 Mixing ratios for synthesis attempts of target compositions with varying Ta starting concentrations, along with various refined parameters with associated goodness of fit ($\chi 2$) values obtained from Rietveld refinement.

Initial Ta at.%	Molar ratios				Composition (actual)	Wt.%	$\chi 2$	Atom (Wyckoff)	z-coordinate	Occupancy			
										M^I		M^{II}	
	TaC	TiC	Ti	Al						Ta	Ti	Ta	Ti
5.0	0.15	1.85	1.0	1.1	$(Ta_{0.05}Ti_{0.95})_3AlC_2$	69.9(6)	2.58	C (4f) Ta,Ti (4f)	0.0774(4) 0.1303(1)	0.07(3)	0.9(1)	0.01(2)	0.99(7)
10.0	0.3	1.7	1.0	1.1	$(Ta_{0.09}Ti_{0.91})_3AlC_2$	35.0(4)	1.60	C (4f) Ta,Ti (4f)	0.0670(7) 0.1310(2)	0.087(2)	0.913(6)	0.104(2)	0.896(8)
20.0	0.6	1.4	1.0	1.1	$(Ta_{0.25}Ti_{0.75})_3Al_{0.77}C_2$	85.3(3)	1.72	C (4f) Ta,Ti (4f)	0.5764(7) 0.1299(1)	0.21(2)	0.79(7)	0.33(2)	0.67(7)
33.3	1.0	1.0	1.0	1.1	$(Ta_{0.38}Ti_{0.62})_3Al_{0.81}C_2$	87.9(2)	1.50	C (4f) Ta,Ti (4f)	0.5719(7) 0.1313(1)	0.340(6)	0.66(2)	0.466(7)	0.53(2)
50.0	1.5	0.5	1.0	1.1	$(Ta_{0.6}Ti_{0.4})_3AlC_2$	-	3.51	C (4f) Ta,Ti (4f)	0.575(5) 0.1323(6)	-	-	-	-

Table S3 Key phase parameters, obtained from Rietveld (XRD) and SAED analysis, for $(Ta_{0.38}Ti_{0.62})_3Al_{0.81}C_2$ and $(Ta_{0.38}Ti_{0.62})_3C_2T_x$ MXene.

Phase	Lattice parameters (Å)				Cell volume (Å^3)**	Impurities	
	a		c			Phase	wt.%
	XRD	SAED	XRD	SAED			
β-$(Ta_{0.05}Ti_{0.95})_3AlC_2$	3.0901(3)	-	18.6005(5)	-	153.82(2)	$(Ta_{0.05}Ti_{0.95})C_x$† Al_2O_3 $TiAl_2$	26.4(3) 2.0(7) 1.7(5)
β-$(Ta_{0.09}Ti_{0.91})_3AlC_2$	3.0862(5)	-	18.584(2)	-	153.29(3)	$(Ta_{0.12}Ti_{0.88})C_x$† Al_2O_3 $TiAl_2$	52.5(3) 4.35(3) 8.20(5)
α-$(Ta_{0.25}Ti_{0.75})_3Al_{0.77}C_2$	3.0951(1)	-	18.5854(6)	-	154.189(8)	$(Ta_{0.24}Ti_{0.76})C_x$† Al_2O_3 $TiAl_2$	8.0(2) 2.20(4) 4.50(9)
α-$(Ta_{0.38}Ti_{0.62})_3Al_{0.81}C_2$	3.0981(1)	3.01(2)	18.6140(7)	18.59(2)	154.745(7)	$(Ta_{0.27}Ti_{0.73})C_x$† Al_2O_3	9.4(2) 2.64(1)
α-$(Ta_{0.6}Ti_{0.4})_3AlC_2$	3.108(1)	-	18.648(7)	-	156.0(1)	(Fig. S4)	-
$(Ta_{0.38}Ti_{0.62})_3C_2T_x$ (pristine)	-	3.14(3)*	-	11.8(1)*	100.3(2)	-	-
$(Ta_{0.38}Ti_{0.62})_3C_2T_x$ (ML)	-	-	19.7(1)	-	-	$(Ta_{0.27}Ti_{0.73})C_x$ †	-
$(Ta_{0.38}Ti_{0.62})_3C_2T_x$ (delaminated)	-	2.97(3) 2.98(3)*	34.9(4)	-	266(4)	$(Ta_{0.27}Ti_{0.73})C_x$ †	-

* From FFT. ** Using XRD values. † C occupancy not determined.

3 X-ray diffraction

For XRD characterisation, MAX phase samples milled to a powder using a TiN-coated bit and then crushed using an agate pestle and mortar. For ML MXene, the powder was scanned after air drying, while for delaminated MXene free standing vacuum filtered films were scanned. XRD scans were carried out using a Rigaku MiniFlex 300/600 diffractometer (Tokyo, Japan) with Cu-K_α radiation (40 kV, 15 mA) incident over a two-theta range of 5-

75° for the MAX phases and 2-70° for MXenes, with a 0.02° step and a dwell time of 0.75 s. Additionally, a 1.25° 10 mm incident slit, a 1.25° 0.3 mm receiving slit, and two 5° Soller slits (incident and receiving) were in place. For the $Ti_3C_2T_z$ sample, XRD scans were performed on a PANalytical X'Pert Pro PW3050/60 (Malvern, UK) with a Cu-K_α source (40 kV, 40 mA) over a two-theta range of 5-70°, 0.033° step size and 1.2 s dwell time. A 2° 10 mm incident beam slit, automatic divergence slit for continuous 10 mm illumination length, and two 2.3° Soller slits (incident and receiving), were also in place.

Spectral phase identification for the MAX phases was performed using relaxed unit cells from computational calculations in Fig. S1 and known phases from the Inorganic Crystal Structure Database (FIZ Karlsruhe GmbH), using CrystalDiffract (CrystalMaker Software Ltd.). Where all major peaks were successfully identified using this method (samples with nominal initial Ta concentrations of 5, 10, 20 and 33.3 at.%.), quantitative phase analysis was performed using the Rietveld refinement method as implemented in the TOPAS software package (Bruker AXS GmbH).[9,10] The refined parameters included: five background parameters, scale factors, X and Y peak width profile parameters, lattice parameters, atomic positions, site occupancies for Ta, Ti and Al, and a single isotropic thermal displacement parameter for all atomic positions in each phase. The relevant Ta:Ti ratio, as obtained from SEM-EDS mapping, was fixed during refinement. For the MXene samples, basal peaks were identified via comparison with the respective MAX phase XRD data and XRD scans of $Ti_3C_2T_x$ MXene. For the sample with a starting Ta concentration of 50 at.%, the Pawley method was used in conjunction to the Rietveld method due to the presence of unidentified phases.[11] Two of the unverified structures 'X' and 'Y' in Fig. S4 are consistent with the $P6_3/mmc$ space group, with lattice parameters of a = 3.041(1) Å, c = 26.24(2) Å for X and a = 2.716(1) Å, c = 21.254(4) Å for Y. The formation of so many phases, none of which appeared to have a distinctly high phase fraction, is evidence that, beyond a certain Ta concentration in the Ti M-layer between 38 and 60 at.%, other MAX phases of 211, 413 or higher order stoichiometry have a higher thermodynamic propensity to form. Another possible culprit for the formation of this variety of higher order and ternary carbide phases is Al: either a deficit of Al in the starting mixture, as higher order MAX phases have higher ratios of MX- to A-layers, or the loss of Al from the newly formed matrix due to the sintering conditions, resulting in phase decomposition. Such behaviour has previously been reported in Ti_3SiC_2 MAX phase, where there is insufficient Si.[12]

All samples analysed with Rietveld refinement contained varying concentrations of two common impurity phases. The first is an F m -3 m structure with lattice parameters lying between those of $(TaTi)C_2$ and TiC, believed to be FCC $(Ta,Ti)C_x$ ($x \leq 2$) with relative Ta/Ti concentrations dependent on the starting composition. In the case of the sample with initial Ta = 10 at.%, this ternary carbide is actually the primary phase at 52.5(3) wt.%, whilst comprising < 10 wt.% in the two phases with high (> 85 wt.%) MAX phase concentration. Measures were employed to minimise the presence of these ternary carbides, such as ball-milling the initial powder mixture for 12 h to encourage uniform elemental distribution, as well as adding excess Al to account for loss from vaporisation during synthesis. However, smaller initial particle sizes may be necessary to further inhibit ternary formation by encouraging solid state diffusion. This is especially relevant for Ta, which has a melting point nearly 1.9 times greater than the furnace temperature employed (1600 °C). The second impurity present is Al_2O_3 which, for the apparatus used in this work, is expected. Despite the use of a Ti oxygen getter, the strongly negative formation enthalpy of Al_2O_3 (-3.44 eV/atom[13]) and small, but inevitable, presence of O_2 leads to preferential and rapid oxidation of exposed elemental Al in the pellet. Another more likely source of oxygen is the native oxide layers present on all metal and carbide particles. To mitigate this, synthesis under high vacuum conditions and/or pre-reducing the starting powders may be required. Additionally, small quantities of $TiAl_2$ (< 8.2 wt.%) were detected in XRD data of β-$(Ta_{0.05}Ti_{2.95})_3AlC_2$, β-$(Ta_{0.09}Ti_{0.91})_3AlC_2$ and α-$(Ta_{0.25}Ti_{0.75})_3Al_{0.77}C_2$.

The disparity between the Ti:Ta ratios in the starting powders and the primary MAX phase matrices can be explained by the presence of the cubic ternary carbide impurities with high Ti concentrations – i.e. $(Ta,Ti)C_x$ ($x \leq 2$). An example of these impurities can be seen in Fig. S6a. Analysis of several impurity particles suggests the Ti:Ta ratio, as well as varying between particles, appears to decrease from a maximum of ~3:1 at the centre, to around 1.4:1 in a thin shell surrounding the particle, before finally increasing to 1.62:1 in the main phase. Whilst the volume fraction of these impurities is low – < 10 wt.% according to XRD data (Table S3), due to the Ti:Ta ratio

reaching almost 3.5:1 for the majority of the particle volume, the mean Ti:Ta ratio across large areas of the sample, including the primary MAX phase is ~2:1.

Despite the measures employed to minimise the presence of these impurity carbides, such as ball-milling the initial powder mixture for 12 hours to encourage isotropic elemental distribution, or adding excess Al to account for loss due to vaporisation during synthesis, smaller initial particle sizes may be necessary to further inhibit formation by encouraging solid state diffusion of elements with low diffusion rates, such as Ta.

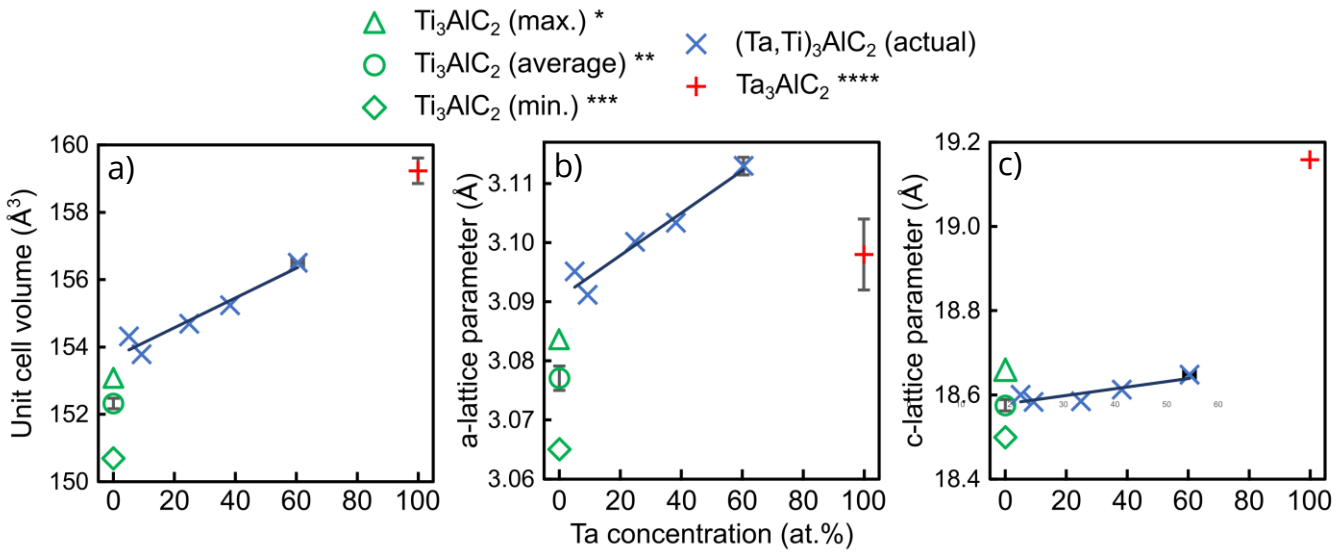

Fig. S3 a) The unit cell volumes, b) *a*-lattice parameters, and c) *c*-lattice parameters of Ti_3AlC_2 (green), $(Ta,Ti)_3AlC_2$ materials from this work (blue) and Ta_3AlC_2 (red). The *x*-axis for all plots is the Ta concentration, in at. %.

* Bei et al.[14], ** [14–21], *** Lane et al.[17], **** Etzkorn et al.[22].

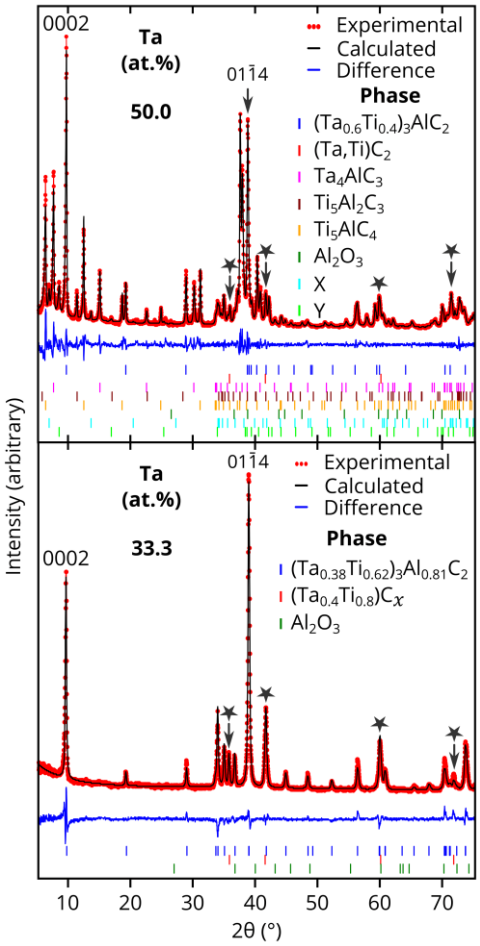

Fig. S5 XRD scans (red spots), with overlaid refinement profiles in black and difference between scan and refined profiles below in blue, of samples with initial M-layer Ta concentrations of a) 50 at.% – with phases included in the Pawley refinement displayed on the right hand side; b) 33.3 at.% – with phases included in the Rietveld refinement profile listed under 'Phase'. For both figures, the (**0002**) and (**01$\bar{1}$4**) peaks of the $(Ta,Ti)_3AlC_2$ phase have been labelled, with peaks representing $(Ta,Ti)C_2$ impurity identified by black stars.

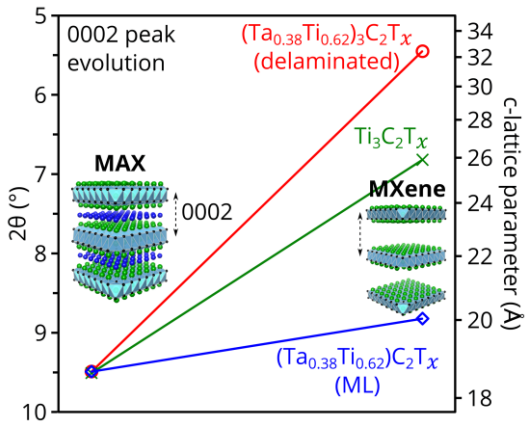

Fig. S4 The (0002) basal peak (left axis) and corresponding *c*-lattice parameter (right axis) evolution from $(Ta_{0.38}Ti_{0.62})_3Al_{0.81}C_2$ as obtained from bulk XRD of delaminated $(Ta_{0.38}Ti_{0.62})_3C_2T_x$ (red), multilayer $(Ta_{0.38}Ti_{0.62})_3C_2T_x$ (blue), and $Ti_3C_2T_x$ partially delaminated with H_2O [23] (green).

4 Electron microscopy

SEM analysis was performed using a FEI Quanta 650 FEG-ESEM operated at an accelerating voltage of 30 kV. The MAX phase samples were mechanically ground and polished to a 1 µm diamond finish prior to analysis. The ML MXene samples were prepared by pressing the powders on a carbon tape mounted on an aluminium stub. Both backscatter electron imaging and EDS quantitative elemental mapping were performed to identify the phases present and to measure the M^{I}:M^{II} ratios in the MAX phase and ternary carbide impurities (Fig. S6).

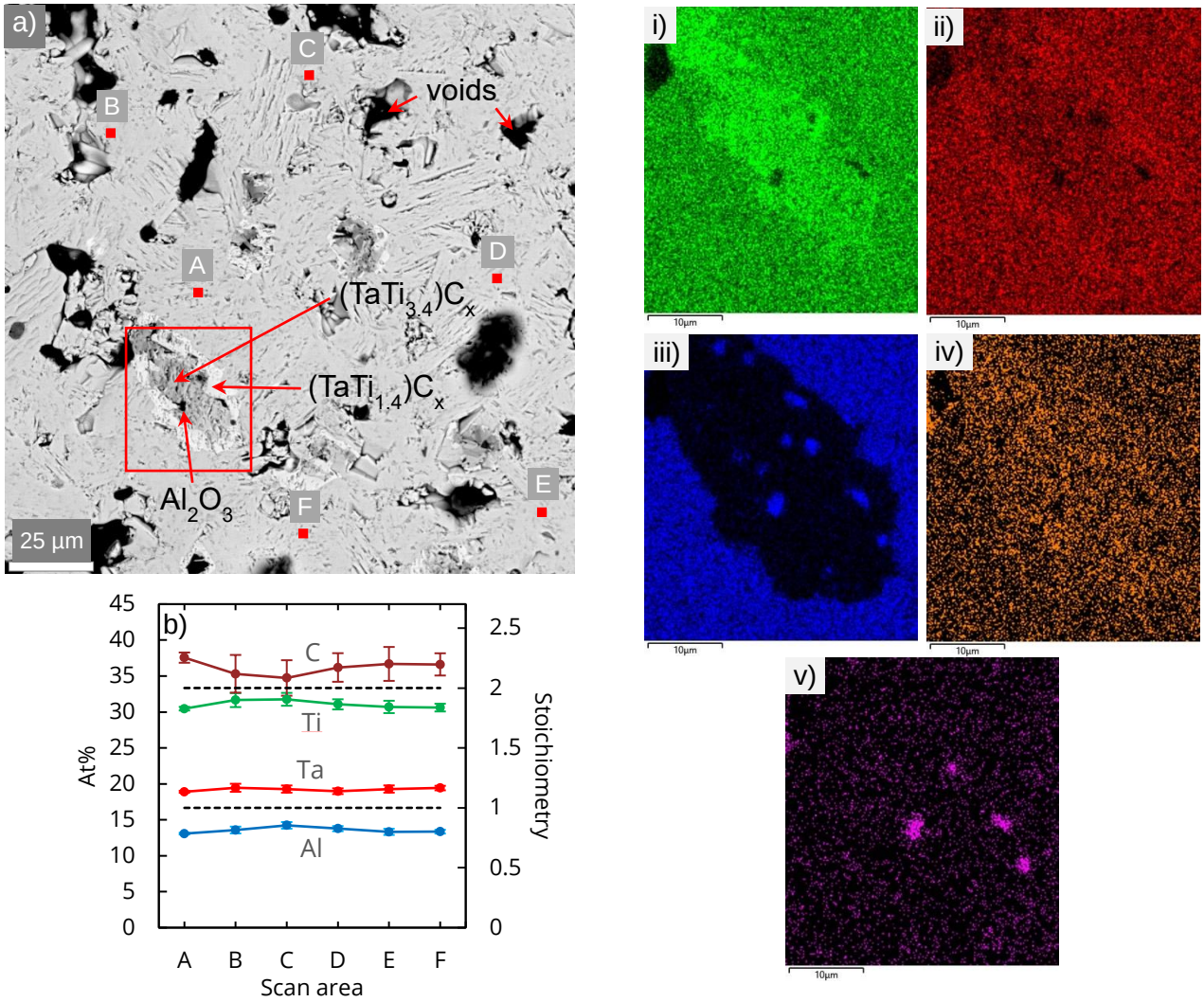

Fig. S6 (a) Backscatter electron SEM micrograph of the surface of as-synthesised $(Ta_{0.38}Ti_{0.62})_3Al_{0.81}C_2$, with EDS scan regions 'A' to 'F' of the MAX phase identified by red squares, and a scan region with a typical impurity particle indicated by the red box, for which X-ray count maps for Ti (green), Ta (red), Al (blue), C (brown) and O (pink) have been shown to the right in (i-v) respectively. (b) Plot of SEM-EDS data from Table S4, with a MAX phase stoichiometry scale included on the right hand y-axis.

Table S4 Normalised elemental concentrations, in at.%, calculated from SEM-EDS measurements of scan areas 'A' to 'F' as indicated in Fig. S6. Apparent MAX phase formulae derived from these measurements are also included.

Scan area	Ti	Ta	Ti/Ta	Al	C	Formula
A	30.5(3)	18.9(1)	1.61(6)	13.1(1)	38(1)	$Ta_{1.15}Ti_{1.85}Al_{0.80}C_{2.31}$
B	30.6(3)	18.8(2)	1.63(5)	13.6(5)	35(3)	$Ta_{1.14}Ti_{1.86}Al_{0.83}C_{2.13}$
C	31.8(9)	19.3(5)	1.7(1)	14.2(5)	35(3)	$Ta_{1.13}Ti_{1.87}Al_{0.83}C_{2.05}$
D	28.7(3)	17.9(2)	1.60(5)	12.6(1)	41(1)	$Ta_{1.15}Ti_{1.85}Al_{0.81}C_{2.64}$
E	31.1(7)	19.0(4)	1.6(1)	13.8(4)	36(2)	$Ta_{1.14}Ti_{1.86}Al_{0.83}C_{2.16}$
F	30.6(5)	19.4(3)	1.58(8)	13.4(3)	37(2)	$Ta_{1.16}Ti_{1.84}Al_{0.80}C_{2.22}$

Electron transparent MAX phase lamellae were prepared for TEM analysis using the focused Ga^+ ion beam *in-situ* lift-out method in an FEI Nova Nanolab 600 SEM.[24] For $(Ta_{0.38}Ti_{0.62})_3Al_{0.81}C_2$, atomic resolution HAADF-STEM images were obtained using a probe corrected FEI Titan G2 with an X-FEG source, operated at 200 kV, with lattice resolution EDS elemental mapping performed using the ChemiSTEM SuperX system on four different scan regions over two lamellae taken from different regions of the bulk sample, providing the range of Ti:Ta ratios reported in the main text. Quantification was performed via the standardless k-factor method and the spectrum images were binned for visual clarity. Binning values of 10 and 4 were used for the spatial and spectral axes respectively. All STEM-EDS processing was performed in HyperSpy,[25] with averaged profiles computed using the NumPy analysis package.[26]

Due to the HAADF detector geometry and sample thickness, the primary source of contrast in the HAADF micrographs is atomic mass (Z) variations. Atoms with a higher Z are more likely to scatter higher angle electrons than lighter ones and, therefore, an increase in HAADF intensity is indicative of an increase in average Z, which in this case refers to an increased Ta concentration (with a Z roughly 3.8 times that of Ti).

MXene TEM samples were prepared by drop-casting colloidally suspended MXene flakes onto a Cu grid with a holey C support film. The grid was then briefly dipped in isopropanol and dried on a hot plate at 80 °C before loading into the TEM. A JEOL ARM300CF STEM at the E02 beamline of the Electron Physical Sciences Imaging Centre (ePSIC) of Diamond Light Source, Ltd. was used for HAADF-STEM imaging 80 kV accelerating voltage, with convergence semi-angles of 32 mrad, and collection inner/outer semi-angle ranges of 68 / 206 mrad. For both the MAX and MXene samples, SAED micrographs were obtained using an FEI Tecnai TF30 FEG-AEM microscope, operating at 300 kV.

Despite the high MAX phase fractions in multiple samples – up to 87.9(2) wt.%, the main phase is itself neither dense nor homogenous. As expected from a pressure-less sintering method, evidence of voids can be seen in SEM micrographs, such as in Fig. S6a. It is possible that these defects exist due to Al failing to intercalate during sintering, or else where Al has been lost at the high temperature following formation, with subsequent decomposition of the HCP MAX phase into an FCC carbide – a process which is known to occur in other MAX phases at high temperatures (> 1000 °C).[27,28]

References

1 G. Kresse and J. Furthmuller, *Phys. Rev. B - Condens. Matter Mater. Phys.*, 1996, **54**, 11169–11186.
2 G. Kresse and J. Furthmiiller, *Comput. Mater. Sci.*, 1996, **6**, 15–50.
3 P. E. Blöchl, *Phys. Rev. B*, 1994, **50**, 17953–17979.
4 J. P. Perdew and Y. Wang, *Phys. Rev. B*, 1992, **45**, 13244.
5 J. P. Perdew, K. Burke and M. Ernzerhof, *Phys. Rev. Lett.*, 1996, **77**, 3865–3868.
6 J. P. Perdew, M. Ernzerhof and K. Burke, *Phys. Rev. Lett.*, 1997, **78**, 3865–3868.
7 Hendrik J. Monkhorst, *Phys. Rev. B*, 1976, **13**, 5188–5192.
8 M. Dahlqvist and J. Rosen, *Nanoscale*, 2020, **12**, 785–794.
9 H. M. Rietveld, *J. Appl. Crystallogr.*, 1969, **2**, 65–71.
10 A. A. Coelho, *J. Appl. Crystallogr.*, 2018, **51**, 210–218.
11 G. S. Pawley, *J. Appl. Crystallogr.*, 1981, **14**, 357–361.
12 M. Griseri, B. Tunca, T. Lapauw, S. Huang, L. Popescu, M. W. Barsoum, K. Lambrinou and J. Vleugels, *J. Eur. Ceram. Soc.*, 2019, **39**, 2973–2981.

13 A. Jain, S. P. Ong, G. Hautier, W. Chen, W. D. Richards, S. Dacek, S. Cholia, D. Gunter, D. Skinner, G. Ceder and K. A. Persson, *APL Mater.*, , DOI:10.1063/1.4812323.
14 G. P. Bei, V. Gauthier-Brunet, C. Tromas and S. Dubois, *J. Am. Ceram. Soc.*, 2012, **95**, 102–107.
15 X. H. Wang and Y. C. Zhou, *J. Mater. Sci. Technol.*, 2010, **26**, 385–416.
16 Y. C. Zhou, J. X. Chen and J. Y. Wang, *Acta Mater.*, 2006, **54**, 1317–1322.
17 N. J. Lane, S. C. Vogel, E. N. Caspi and M. W. Barsoum, *J. Appl. Phys.*, , DOI:10.1063/1.4803700.
18 M. A. Pietzka and J. C. Schuster, *J. Phase Equilibria*, 1994, **15**, 392–400.
19 N. V Tzenov and M. W. Barsoum, *Am. Ceram. Soc*, 2000, **83**, 825–32.
20 N. J. Lane, M. Naguib, J. Lu, L. Hultman and M. W. Barsoum, *J. Eur. Ceram. Soc.*, 2012, **32**, 3485–3491.
21 T. Yang, C. Wang, W. Liu, S. Liu, J. Xiao, Q. Huang, J. Xue, S. Yan and Y. Wang, *Acta Mater.*, 2017, **128**, 1–11.
22 J. Etzkorn, M. Ade and H. Hillebrecht, *Inorg. Chem.*, 2007, **46**, 1410–1418.
23 L. Verger, V. Natu, M. Carey and M. W. Barsoum, *Trends Chem.*, 2019, 1, 656–669.
24 F. A. Stevie, C. B. Vartuli, L. A. Giannuzzi, T. L. Shofner, S. R. Brown, B. Rossie, F. Hillion and R. H. Mills, *Surf. Interface Anal.*, 2001, **31**, 345–351.
25 F. de la Peña, E. Prestat, V. T. Fauske, P. Burdet, P. Jokubauskas, M. Nord, T. Furnival, T. Ostasevicius, K. E. MacArthur, D. N. Johnstone, M. Sarahan, J. Lähnemann, J. Taillon, pquinn-dls, V. Migunov, A. Eljarrat, T. Aarholt, J. Caron, S. Mazzucco, B. Martineau, S. Somnath, T. Poon, M. Walls, T. Slater, F. Winkler, N. Tappy, G. Donval, J. C. Myers, R. McLeod and E. R. Hoglund, 2020.
26 S. van der Walt, S. C. Colbert and G. Varoquaux, *Comput. Sci. Eng.*, 2011, **13**, 22–30.
27 W. K. Pang, I. M. Low, B. H. O'Connor, A. J. Studer, V. K. Peterson, Z. M. Sun and J. P. Palmquist, *J. Phys. Conf. Ser.*, , DOI:10.1088/1742-6596/251/1/012025.
28 I. M. Low and W. K. Pang, *Key Eng. Mater.*, 2014, **617**, 153–158.